

1 **Ice shelf basal melt rates in the Amundsen Sea at the**  
2 **end of the 21<sup>st</sup> century**

3 **Nicolas C. Jourdain<sup>1</sup>, Pierre Mathiot<sup>1</sup>, Clara Burgard<sup>1</sup>, Justine Caillet<sup>1</sup>,**  
4 **Christoph Kittel<sup>1</sup>**

5 <sup>1</sup>Univ. Grenoble Alpes/CNRS/IRD/G-INP, Institut des Géosciences et de l'Environnement, Grenoble,  
6 France

7 **Key Points:**

- 8 • We present 1/12° ocean–sea-ice–ice-shelf projections at the end of the 21<sup>st</sup> cen-  
9 tury under the RCP8.5 scenario.  
10 • Ice shelf melt rates in the Amundsen Sea are typically multiplied by 1.4 to 2.2 from  
11 1989–2009 to 2080–2100.  
12 • Advection of warmer water from remote locations and reduced Ekman downwelling  
13 are the main drivers of changes in ice shelf melt rates.

---

Corresponding author: Nicolas C. Jourdain, [nicolas.jourdain@univ-grenoble-alpes.fr](mailto:nicolas.jourdain@univ-grenoble-alpes.fr)

## Abstract

Antarctic Ice Sheet projections show the highest sensitivity to increased basal melting in the Amundsen Sea sector. However, little is known about the processes that control future increase in melt rates there. We build an ensemble of three ocean–sea-ice–ice-shelf simulations for both the recent decades and the late 21<sup>st</sup> century, constrained by regional atmosphere simulations and the multi-model mean climate change of the 5<sup>th</sup> Climate Model Intercomparison Project under the RCP8.5 scenario. The ice shelf melt rates are typically multiplied by 1.4 to 2.2 from present day to future, for a total basal mass loss increased by 347 Gt yr<sup>-1</sup>. This is approximately equally explained by advection of warmer water from remote locations and by regional changes in Ekman downwelling and in the ice-shelf melt-induced circulation, while increased iceberg melt plays no significant role. Our simulations suggest that high-end melt projections previously used to constrain recent sea level projections may have been significantly overestimated.

## Plain Language Summary

Future sea level rise highly depends on how fast the ocean will melt the floating ice shelves in Antarctica, which modulates the ice flow from the ice sheet into the ocean. This is particularly true for the Amundsen Sea sector where the ice flow into the ocean is very sensitive to ocean-induced melting. Here we use a numerical model that represents the evolution of the Amundsen Sea, including under the floating ice shelves. Under a high-end greenhouse-gases concentration pathway, our simulations indicate that melt rates beneath the ice shelves may increase by 40 to 120%. This is explained by both warmer seawater coming from distant regions and changes in the local wind stress. Our simulations suggest that high-end melt projections previously used to constrain recent sea level projections may have been overestimated.

## 1 Introduction

Most projections of the Antarctic contribution to sea level rise are based on standalone ice sheet models in which melting beneath ice shelves is parameterized (Levermann et al., 2020; Seroussi et al., 2020; DeConto et al., 2021; Edwards et al., 2021). The existing melt parameterizations are based on highly simplified representations of the ocean circulation and heat exchanges in ice shelf cavities, and the resulting melt rates are significantly biased (Favier et al., 2019; Burgard et al., 2022). Furthermore, these melt parameterizations are typically driven by ocean warming derived from simulations of the Climate Model Intercomparison Project (CMIP, Eyring et al., 2016), although ice shelf cavities are not represented and ocean properties on the Antarctic continental shelf are significantly biased (Purich & England, 2021).

To either trust or challenge these ice sheet and sea level projections, our community needs projections that resolve the ocean dynamics over the Antarctic continental shelf and beneath the ice shelves, but such projections are rare (Asay-Davis et al., 2017). Timmermann and Hellmer (2013) and Naughten et al. (2018) pioneered CMIP-based projections at the Antarctic scale, using a global ocean model with refined resolution around Antarctica and beneath ice shelves. Their projections were nonetheless of limited use for the Amundsen Sea sector because of a substantial cold bias in their present-day state. Siahbaan et al. (2021) were the first to run a global climate model (i.e., land, ocean, atmosphere) with an interactive Antarctic Ice Sheet in scenario-based projections. Their present-day melt rates were reasonable in the Amundsen Sea, but they found little change in their projections and questioned the representation of the Amundsen cavities at their resolution (e.g., only 11 grid columns for Pine Island ice shelf cavity). Stronger present-day biases were nonetheless found at higher ocean resolution in their model configuration (Smith et al., 2021).

63 Given that the Antarctic Ice Sheet projections show the highest sensitivity to in-  
 64 creased basal melting in the Amundsen Sea sector (together with the Wilkes Land sec-  
 65 tor, Seroussi et al., 2020), it seems crucial to better estimate possible future ice shelf melt  
 66 rates in that region and describe the associated mechanisms. Recent simulations of the  
 67 Amundsen Sea by Naughten et al. (2022) have shown that relatively warm periods be-  
 68 come more dominant over the 20<sup>th</sup> century, causing stronger ice shelf melting. In this  
 69 paper, we use a regional ocean–sea-ice–ice-shelf model to build new projections to 2100  
 70 under the RCP8.5 scenario for the Amundsen Sea region and to describe the mechanisms  
 71 explaining changes in ice shelf melt rates. High-end sea level projections are  
 72 needed from an adaptation perspective (Hinkel et al., 2019; Durand et al., 2022), but are  
 73 currently extremely uncertain, partly due to the poorly constrained sensitivity of ice shelf  
 74 melt rates to ocean warming (Fox-Kemper et al., 2021; Edwards et al., 2021). This is  
 75 our motivation to focus on the RCP8.5 scenario, which is on the higher end of possible  
 76 scenarios in a world with no climate policy (Hausfather & Peters, 2020a, 2020b). Finally,  
 77 we use our ocean projections to assess existing melt parameterizations recently used in  
 78 ice sheet projections.

## 79 2 Ocean–sea-ice–ice-shelf simulations

80 We make use of the NEMO-3.6 (Nucleus for European Modelling of the Ocean, Madec  
 81 & NEMO-team, 2016) ocean model that includes the LIM3 (Louvain Ice Model, Rous-  
 82 set et al., 2015) sea ice model and the ice shelf cavity module developed by Mathiot et  
 83 al. (2017). The grid extends from 142.1°W to 84.9°W and from 76.5°S to 59.7°S, and has  
 84 a resolution of 1/12° in longitude, i.e., a quasi-isotropic resolution varying from 4.7 km  
 85 at the northern boundary to 2.2 km in the southernmost part of the domain. We use 75  
 86 vertical levels of thickness ranging from 1 m at the surface to 204 m at 6000 m depth,  
 87 and a typical thickness of 30 to 100 m for ocean cells beneath ice shelves. Unless stated  
 88 otherwise, the parameters are those used in Jourdain et al. (2017) and the complete set  
 89 of NEMO parameters is provided on <https://doi.org/10.5281/zenodo.6644859>.

90 To get a rough estimate of the model uncertainty, we run an ensemble of three present-  
 91 day and future simulations. For ensemble member A, the ice shelf and seabed topogra-  
 92 phy is extracted from BedMachine-Antarctica-v1.33 (Morlighem et al., 2020), while mem-  
 93 bers B and C are based on BedMachine-Antarctica-v2.0 (Morlighem, 2020). Addition-  
 94 ally, B and C include a representation of grounded tabular icebergs, in particular B22A  
 95 (Antarctic Iceberg Tracking Database, Budge & Long, 2018), whose ungrounded parts  
 96 are treated as an ice shelf, and the line of icebergs grounded on Bear Ridge (Nakayama  
 97 et al., 2014; Bett et al., 2020). The ocean–ice-shelf heat exchange coefficient ( $\Gamma_T$ ) is  $2.21 \times$   
 98  $10^{-2}$  in A vs  $1.88 \times 10^{-2}$  in B-C, while the ocean–ice-shelf salt exchange coefficient is  
 99 always defined as  $\Gamma_S = \Gamma_T/35$ . Finally, two parameters of the sea ice model differ: the  
 100 maximum permitted sea ice concentration is set to 99.9% of the mesh in A-B vs 95% in  
 101 C, and the ice–ocean drag coefficient is set to  $5.0 \times 10^{-3}$  in A-B vs  $2.5 \times 10^{-3}$  in C. All  
 102 these parameter values are commonly used in the NEMO community. Our ensemble is  
 103 designed to simply illustrate the importance of a few empirical choices and cannot be  
 104 considered as a deep exploration of NEMO’s parametric uncertainty (e.g., Williamson  
 105 et al., 2017).

106 Our present-day simulations cover 1989–2009, following 10 years of spin up from  
 107 1979. The surface boundary conditions consist of 3-hourly (temperature, humidity, wind  
 108 velocity) and daily (radiative fluxes and precipitation) mean outputs of the 10 km MAR  
 109 (Regional Atmospheric Model, Gallée & Schayes, 1994) configuration described and eval-  
 110 uated by Donat-Magnin et al. (2020). The lateral ocean and sea ice boundary conditions  
 111 consist of 5-day mean outputs of a global 0.25° NEMO simulation very similar to the one  
 112 described by Merino et al. (2018) except that it is spun up from 1958 and that the im-  
 113 posed ice shelf melt flux increases linearly from 1990 to 2005 and is constant before and  
 114 after that, with values corresponding to the FRESH– and FRESH+ reconstructions of

115 Merino et al. (2018). The global  $0.25^\circ$  simulation represents Lagrangian icebergs (Merino  
116 et al., 2016), and their 5-day averaged melt rate (Jourdain, Merino, et al., 2019) is ap-  
117 plied at the surface of our regional  $1/12^\circ$  configuration. In addition, seven tidal constituents  
118 are applied at the lateral boundaries as in (Jourdain, Molines, et al., 2019). Our present-  
119 day simulations are evaluated in sup. section S1. In summary, our simulations are too  
120 warm at depth by approximately  $0.5^\circ\text{C}$ , and ice shelf melt rates are consequently slightly  
121 overestimated.

122 Our future simulations cover 2080–2100 and are representative of the CMIP5 multi-  
123 model mean under the RCP8.5 concentration pathway. The surface boundary conditions  
124 are taken from the MAR regional projections described and evaluated through a perfect-  
125 model approach in Donat-Magnin et al. (2021). The atmospheric projections themselves  
126 were driven at their surface and lateral boundaries by the mean seasonal anomalies (2080–  
127 2100 minus 1989–2009) derived from 33 CMIP5 models under the RCP8.5 scenario (more  
128 details are provided in Donat-Magnin et al., 2021). Our future simulations start from  
129 the 1979 ocean conditions (same as present-day), and are spun up for 10 years under warm  
130 conditions using the same method as for 2080–2100. Due to its open lateral boundaries,  
131 our regional ocean model configuration is no longer sensitive to its initial state after ap-  
132 proximately seven years (Jourdain et al., 2017), which means that starting our future  
133 runs from the present-day conditions is acceptable as long as we allow some years for spin  
134 up, and it is not required to simulate the entire 2010–2070 period to estimate melt rates  
135 at the end of the 21<sup>st</sup> century.

136 The applied anomalies induce an eastward zonal wind and sea ice stress anomaly  
137 along the shelf break and offshore (Fig. 1a,b), which is a known response of the CMIP  
138 models to high greenhouse gases concentrations by 2100 (Swart & Fyfe, 2012; Holland  
139 et al., 2019; Goyal et al., 2021). We also find an increased westward stress along most  
140 of the ice sheet margin (Fig. 1b), which is possibly related to higher air temperature gra-  
141 dient across the ice-sheet–ocean boundary in the presence of reduced sea ice cover in the  
142 future. On average over the continental shelf, the Ekman downward velocity due to the  
143 wind and sea ice stress is weakened by 50% in the future compared to present day (sup.  
144 section S2).

145 In terms of surface heat fluxes, the Amundsen continental shelf loses 41% less en-  
146 ergy to the atmosphere in the future compared to present-day (Fig. 1c,d), which is con-  
147 sistent with the effect of a warmer troposphere on downward sensible and longwave heat  
148 fluxes over the open ocean and sea ice. Precipitation increases by 22% (Fig. 1e,f) due  
149 to a higher water holding capacity of the troposphere in a warmer climate (Donat-Magnin  
150 et al., 2021). The increased precipitation and the reduced sea ice production over the  
151 continental shelf (from  $0.23$  to  $0.19$   $\text{Gt yr}^{-1}$ ) are together responsible for an annual rate  
152 of surface buoyancy loss reduced by 75% in the future compared to present day (supp.  
153 section S2).

154 We adopt a similar approach for the lateral boundaries of our regional ocean–sea-  
155 ice simulations and add the CMIP5 multi-model mean seasonal anomalies to the present-  
156 day lateral boundary conditions (for temperature, salinity, ocean velocity, sea ice con-  
157 centration, sea ice thickness, and snow-on-ice thickness). The perturbation applied at  
158 our lateral boundaries is comprehensively described in sup. section S3, which can be sum-  
159 marised as a warming that exceeds  $0.25^\circ\text{C}$  everywhere in the first 1000 m and reaches  
160  $2^\circ\text{C}$  in the northernmost part of our domain, as well as a freshening of the first 100 m  
161 that is particularly pronounced near the Antarctic coast.

162 Two additional sensitivity experiments are performed for further insight into the  
163 processes. First, we repeat the future simulation of ensemble member B but we only ap-  
164 ply the future surface forcing, i.e., we keep the present-day lateral boundary conditions  
165 for ocean and sea ice. Second, we repeat the future simulation of ensemble member C  
166 but with increased iceberg melting (which is kept at present-day values in the other ex-

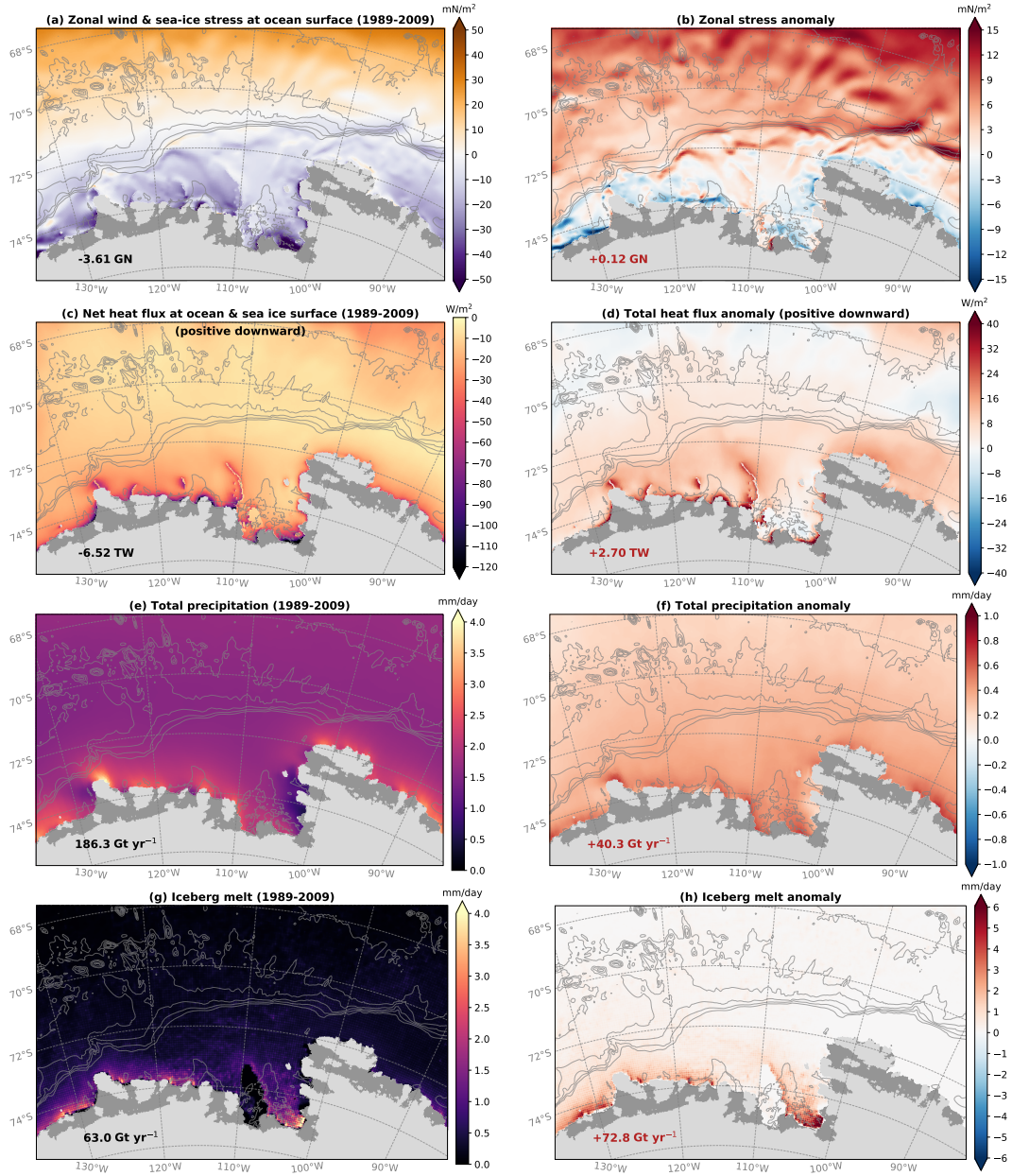


**Figure 1.** Present-day atmospheric forcing (left) and future anomalies with respect to present day (right). Anomalies are calculated as the average of 2080–2100 minus 1989–2009. The grounded ice sheet and the ice shelves are shaded in light and dark grey, respectively. The grey contours indicate the bathymetry (every 750 m). Numbers near the lower left corner indicate the value of the plotted field integrated over the continental shelf, which is defined as the area between the 1500 m isobath and the coastline, and between 100°W and 135°W.

167 periments). Following the calculations presented in section S4, we increase the total ice-  
 168 berg melt flux over the Amundsen continental shelf from  $63 \text{ Gt yr}^{-1}$  at present-day to  
 169  $136 \text{ Gt yr}^{-1}$  at the end of the 21st century under RCP8.5 (Fig. 1g,h).

### 170 **3 Results: changes in ice shelf basal melting and related processes**

171 On average over the three ensemble members, the ice shelf melt rates are multi-  
 172 plied by 1.4 to 2.2 (depending on the ice shelf) from present day to future (Fig. 2a). The  
 173 total ice shelf meltwater flux in the Amundsen Sea increases by  $347 \text{ Gt yr}^{-1}$  on average  
 174 (Fig. 2b,c), with a standard deviation of  $54 \text{ Gt yr}^{-1}$  across the ensemble.

175 Interestingly, members B and C give almost identical future melt rates while present-  
 176 day values differ significantly (Fig. 2a). As the only difference between B and C is the  
 177 set of sea ice parameters, this indicates that sea ice production and the related surface  
 178 buoyancy flux are important drivers of ice shelf melting presently, but no longer play a  
 179 role in the future. This is very likely related to both the 75% reduction of the surface  
 180 buoyancy loss in the future and the mixing of more ice shelf meltwater into the surface  
 181 layer. Both increase the ocean stratification and prevent surface waters from reaching  
 182 deeper warmer layers on the continental shelf through convective mixing. We also do not  
 183 find any significant difference between projection C with and without increased iceberg  
 184 melt rates (not shown), which supports the idea of a decoupling between the surface and  
 185 the deeper layers in the future.

186 The changes in melt rates for member B without perturbations of NEMO's lateral  
 187 boundaries are shown by the white disruption of the middle brown bars in Fig. 2a. In-  
 188 creased melt rates underneath Abbot and Venable ice shelves are almost entirely explained  
 189 by the modified lateral boundary conditions. For the other ice shelves, the part of in-  
 190 creased melt rate attributed to the lateral boundaries varies from  $1/3$  to  $2/3$  of the to-  
 191 tal change, depending on the ice shelf. This indicates that future changes in remote ocean  
 192 properties are important, i.e., local changes in the atmospheric forcing cannot entirely  
 193 explain the projected increase in ice shelf melt rates.

194 We then use the terms of the exact heat and salt budget (saved online and calcu-  
 195 lated as in Jourdain et al., 2017) to get further insights into the physical mechanisms.  
 196 The offshore projection is characterised by a  $0.25^\circ\text{C}$  warming below the thermocline due  
 197 to horizontal advection from the domain boundaries, a 75 m higher thermocline explained  
 198 by horizontal advection and decreased convective mixing due to less sea ice formation,  
 199 and a surface freshened by  $0.4 \text{ g kg}^{-1}$  (Fig. S6 and its description in sup. section S4).  
 200 Changes over the continental shelf are more intense, with  $0.5^\circ\text{C}$  warming at depth, a 160 m  
 201 higher thermocline (Fig. 3a), and surface freshened by  $0.5 \text{ g kg}^{-1}$  (Fig. 3b). In contrast  
 202 to the offshore mechanisms, vertical advection plays a key role on the continental shelf  
 203 (Fig. 3c,d). Approximately half of the heat brought by changes in vertical advection be-  
 204 tween 250 and 800 m is due to the melt-induced circulation in ice shelf cavities and is  
 205 mostly consumed as latent heat for ice melting (compare Fig. 3c,d to Fig. 3e,f). The re-  
 206 maining part is consistent with the reduced Ekman downwelling described in the pre-  
 207 vious section and in Spence et al. (2014) and Naughten et al. (2022), which reduces the  
 208 downward advection of relatively cold and fresh water from the surface layer (above 250 m)  
 209 to deeper layers (Fig. 3c,d). A closer look at the budget terms within ice shelf cavities  
 210 (not shown) reveals an additional input of heat and freshwater between 100 and 400 m  
 211 depth corresponding to the melt-induced circulation that releases a mixture of meltwa-  
 212 ter and entrained Circumpolar Deep Water (CDW) at the ice shelf front as described  
 213 by Jourdain et al. (2017).

214 The strong freshening of the surface layer (above 250 m) is dominated by increased  
 215 ice shelf melting. Out of the  $347 \text{ Gt yr}^{-1}$  of additional ice shelf meltwater, only  $51 \text{ Gt yr}^{-1}$   
 216 are injected directly into the surface layer, but the absence of sub-surface freshening (Fig. 3b)

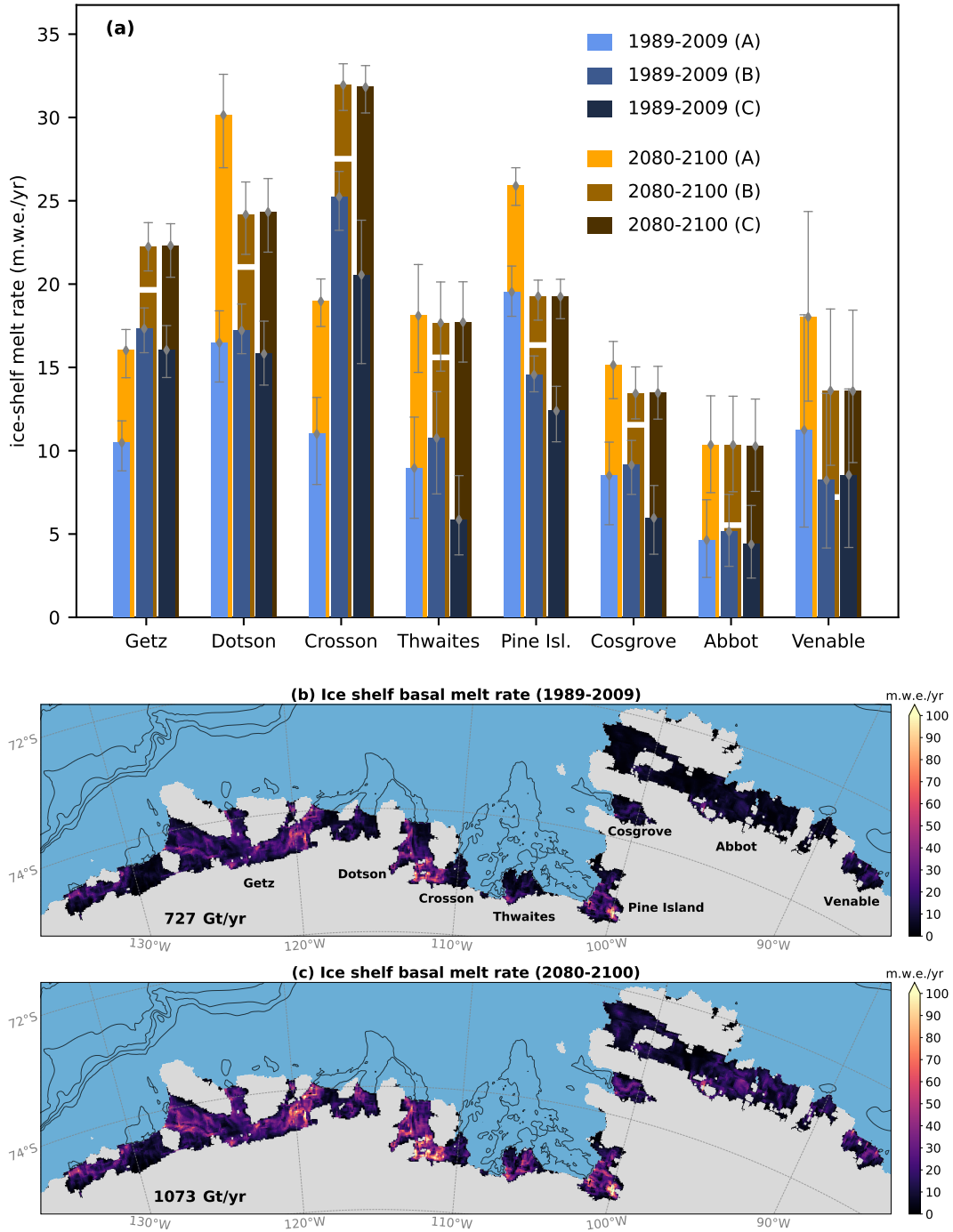


**Figure 2.** (a) Mean present day and future melt rates of individual ice shelves in model configurations A, B and C (in meters of liquid water equivalent per year, i.e.  $10^3 \text{ kg m}^{-2} \text{ yr}^{-1}$ ). The grey bars cover 95% of the monthly values, i.e. between the 2.5<sup>th</sup> and the 97.5<sup>th</sup> percentiles. The white disruption of the light brown bars (B over 2080-2100) represent the future melt rate in the experiment with lateral boundary conditions kept at present-day values. (b,c) Present-day and future ice shelf melt rates, and integrated value over the domain in the lower left corner. The black contours indicate the bathymetry (every 750 m).

217 and the examination of the role of vertical advection in Fig. 3d,f indicate that most of  
 218 the additional ice shelf meltwater is transported towards the surface layer. These addi-  
 219 tional  $347 \text{ Gt yr}^{-1}$  are much larger than the  $73 \text{ Gt yr}^{-1}$  of increased iceberg melting (Fig. 1h),  
 220  $40 \text{ Gt yr}^{-1}$  of increased precipitation (Fig. 1f), and a sea ice production decreased by  $37 \text{ Gt yr}^{-1}$   
 221 which is equivalent to a freshwater release of  $30 \text{ Gt yr}^{-1}$  (for a sea ice salinity of  $6.3 \text{ g kg}^{-1}$ ).

#### 222 4 Results: assessment of simple ice shelf melt parameterizations

223 Here we use our NEMO projections to assess the non-local (also referred to as semi-  
 224 local) quadratic parameterization proposed by Favier et al. (2019) and used in some of  
 225 the standard ice sheet projections of the Ice Sheet Model Intercomparison Project for  
 226 CMIP6 (ISMIP6, Nowicki et al., 2020; Seroussi et al., 2020), with a melt rate defined  
 227 as:

$$m(x, y) = K \times (TF(x, y, z_{\text{draft}}) + \delta T) \times |\langle TF \rangle_{\text{ice-shelf}} + \delta T| \quad (1)$$

228 where  $TF(x, y, z_{\text{draft}})$  is the thermal forcing at the ice-ocean interface of depth  $z_{\text{draft}}$ , and  
 229  $\langle TF \rangle_{\text{ice-shelf}}$  the thermal forcing averaged over an entire ice shelf draft. The temperature  
 230 correction  $\delta T$  is used to correct biases in present-day observations and to account for melt-  
 231 induced cooling or other poorly represented processes (Jourdain et al., 2020).  $K$  is a tun-  
 232 ing coefficient that was expressed in various ways across previous studies. An expression  
 233 of  $K$  was proposed by Favier et al. (2019) and Jourdain et al. (2020), but we find the  
 234 expression proposed by Jenkins et al. (2018) and Burgard et al. (2022) more physically  
 235 sound. For ISMIP6, Jourdain et al. (2020) proposed two calibration methods, one re-  
 236 ferred to as "MeanAnt", ensuring realistic present-day melt rates at the scale of Antarc-  
 237 tica for minimal temperature corrections and giving  $K_{\text{MeanAnt}} = 2.57 \text{ m yr}^{-1} \text{ K}^{-2}$ , and  
 238 the other one referred to as "PIGL", ensuring more realistic present-day melt rates near  
 239 Pine Island's grounding line and giving  $K_{\text{PIGL}} = 28.2 \text{ m yr}^{-1} \text{ K}^{-2}$ , but requiring neg-  
 240 ative  $\delta T$  corrections almost everywhere to keep reasonable melt rates for individual ice  
 241 shelves or integrated over larger sectors.

242 In the following, we assume that the present-day temperature is perfectly known,  
 243 so that we can use  $\delta T = 0$  for MeanAnt and we find that present-day RMSE from PIGL  
 244 are lowest for  $\delta T = -1.9^\circ\text{C}$ . For clarity, we just show the results for Pine Island and  
 245 Thwaites (Fig. 4), which are key ice shelves for the Antarctic contribution to sea level  
 246 rise, but the other ice shelves have a very similar behaviour. We estimate the future pa-  
 247 rameterized melt rates in two ways: (1) from the future ocean temperatures simulated  
 248 by NEMO (orange dashed curves in Fig. 4), and (2) from the CMIP5 multi-model mean  
 249 ocean warming added to the NEMO present-day temperatures (dashed dark red curves  
 250 in Fig. 4) which corresponds to what is commonly used in standalone ice sheet projec-  
 251 tions like ISMIP6.

252 First of all, the present-day parameterized melt rates overall agree with NEMO al-  
 253 though the exact vertical distribution is only poorly captured (blue curves in Fig. 4). The  
 254 MeanAnt curves show some overlap between the three model projections and the 90<sup>th</sup>  
 255 confidence interval of the parameterized projections (orange curves in Fig. 4a,b), although  
 256 the RMSE approximately doubles compared to present day. The PIGL projections are  
 257 much worse, with very little overlap between the three model projections and the 90<sup>th</sup>  
 258 confidence interval of the parameterized projections (orange curves in Fig. 4c,d). For the  
 259 95<sup>th</sup> percentile of  $K$ , the maximum melt rates in either Pine Island or Thwaites cavity  
 260 are overestimated by a factor of five. The melt projections directly based on the CMIP5  
 261 ocean warming (dashed dark red curves in Fig. 4) are similar to the projections from the  
 262 warming produced by NEMO, indicating that most of the bias comes from the param-  
 263 eterization itself.

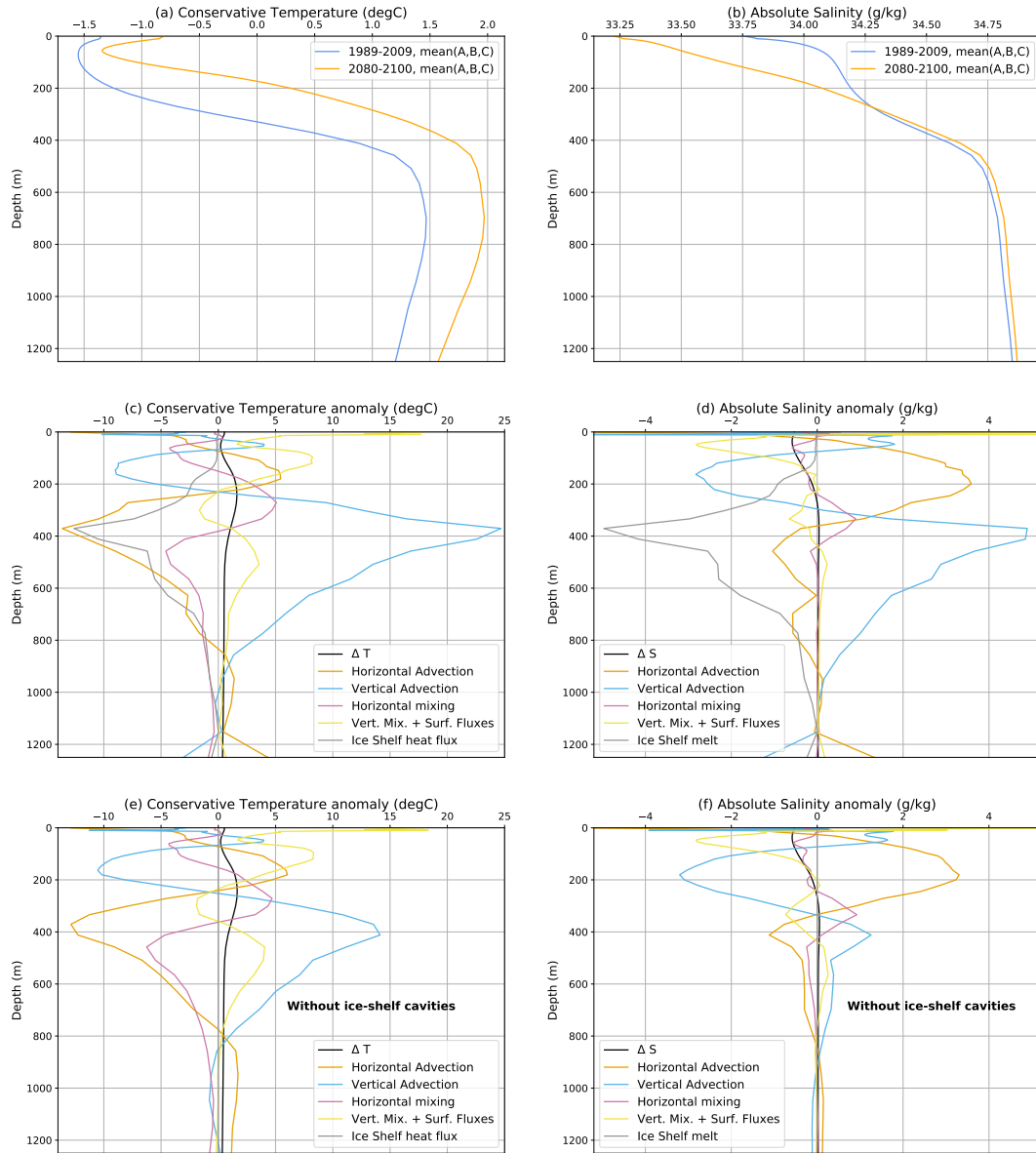


**Figure 3.** (a,b) Present-day and future conservative temperature and absolute salinity profiles over the Amundsen Sea continental shelf (defined as the area between the 1500 m isobath and the coastline, and between 100°W and 135°W), including ice shelf cavities. (c,d) temperature ( $\Delta T$ ) and salinity ( $\Delta S$ ) change from present-day to future conditions and contributions of the individual terms of the heat and salt equations to  $\Delta T$  and  $\Delta S$ , respectively. The individual tendency terms of the heat and salt equations were integrated in time from the initial state until each month of either 1989-2009 or 2080-2100, then averaged over each of these 20-year period, from which we extracted the difference between the two periods (similar to equations 6 and 7 of Jourdain et al., 2017). (e,f) same as (c,d) but excluding ice shelf cavities from the heat and salt budget calculation.

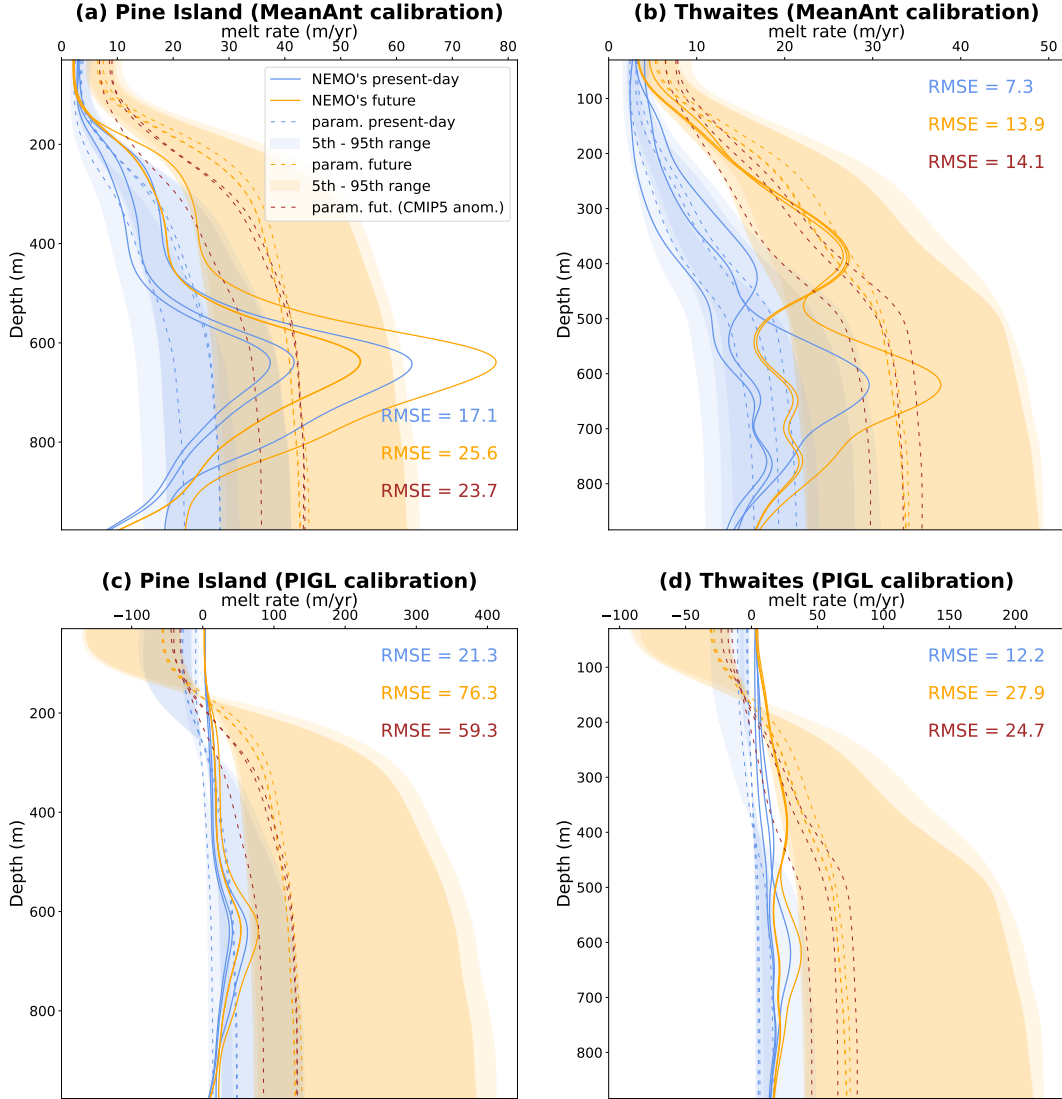


**Figure 4.** Melt profiles beneath Pine Island (left) and Thwaites (right) ice shelves, from the NEMO simulations (solid lines), and from the ISMIP6 standard parameterization (dashed lines) tuned following either the "MeanAnt" (upper panels) or the "PIGL" (lower panels) method (median  $K$  coefficient derived from Jourdain et al., 2020). The present day parameterized melt rates are based on NEMO's present-day temperatures in front of the ice shelf cavities (within 50 km from the ice shelf front). The future melt rate is either calculated from the's future temperatures simulated by NEMO (orange dashed lines) or from the CMIP5 multi-model mean temperature anomaly (dark red dashed lines). The semi-transparent shaded areas indicate the range corresponding to the 5<sup>th</sup> and 95<sup>th</sup> percentiles of  $K$  coefficients based on the future temperatures produced by NEMO (values derived from Tab. 2 of Jourdain et al. 2020). The three curves for each estimate correspond to the three members of our small ensemble. Every curve is built using a kernel density estimate based on a Gaussian function of standard deviation equal to 1/20<sup>th</sup> of the maximum ice draft depth. The Root Mean Square Errors (RMSE, in m/yr) are calculated for the spatial pattern with regards to the NEMO values and correspond to the median  $K$  values.

## 5 Discussion and conclusion

In this paper, we have built an ensemble of three  $1/12^\circ$  ocean–sea-ice–ice-shelf projections of the late 21<sup>st</sup> century under the RCP8.5 concentration pathway. In these simulations, the net surface buoyancy loss is reduced by 75% in the future compared to present day due to surface freshening by increased precipitation, increased iceberg melt and reduced sea ice production. Increased ice shelf melt also contributes greatly to making the surface layer fresher and more buoyant in the future. The result is a decoupling between the surface layer and deeper layers on the continental shelf, which makes future ice shelf melt insensitive to additional perturbations of surface buoyancy fluxes. We find that the future Ekman downwelling velocity is reduced by half over the continental shelf compared to present day. This, in addition to the melt-induced circulation, largely explains the additional heat made available to ice shelf melting. However, regional changes in atmospheric forcing only explain 1/3 to 2/3 of the increase in ice shelf melt rates (depending on the ice shelf). The remaining is due to advection of warmer water from remote locations (i.e. from our model domain lateral boundaries). The importance of advection from remote locations was already evidenced by Nakayama et al. (2018) for the interannual variability of the Amundsen Sea. Here we clearly show the caveats of attributing future changes in ice shelf melting to regional atmospheric perturbations in the Amundsen Sea (e.g., Holland et al., 2019).

The relative changes in melt rates (+48% for all simulated ice shelves, Fig. 2b,c) are lower than previous estimates, e.g., +189% until 2100 in the Amundsen Sea for the CMIP5 multi-model mean under RCP8.5 in Naughten et al. (2018) and +250% until 2100 for Pine Island under the A1B and E1 scenarios in Timmermann and Hellmer (2013). The present-day melt rates were strongly underestimated in these previous studies, due to a cold bias that suggests overestimated deep convection related to overestimated sea ice production and/or too weak vertical density stratification (e.g. from underestimated precipitation). Such a cold Amundsen Sea is therefore very sensitive to changes in surface heat and buoyancy fluxes that can induce a transition from sea-floor temperatures near the surface freezing point to much warmer conditions typical of the presence of CDW. In our case, we start from a more realistic state with weakly modified CDW on the continental shelf, so that important warming at depth cannot be triggered by surface heat and buoyancy fluxes, and the Ekman dynamics is the main driver of changes in ice shelf melt rates. We nonetheless acknowledge that our  $0.5^\circ\text{C}$  warm bias may lead to an underestimation of present-day episodic convection, leading to an underestimation of the ocean warming and relative increase in ice shelf melt rates. For a given ocean warming, starting from cold biased conditions also produces important relative changes in melt rates because the calculation of relative change involves a division by the initial thermal forcing. For example, assuming a quadratic dependency of melt to the thermal forcing (Holland et al., 2008),  $0.5^\circ\text{C}$  of future warming at 600 m depth would correspond to melt rates increased by 143% starting from the  $-2.6^\circ\text{C}$  bias of Naughten et al. (2018), by 30% starting from an observed temperature of  $1.0^\circ\text{C}$  (Dutrieux et al., 2014) and by 26% (starting from our simulations with a  $+0.5^\circ\text{C}$  bias).

Our projection method is innovative in the sense that it enables a representation of the CMIP multi-model mean at relatively high resolution and with basic bias correction. We have chosen to drive our projections directly by the CMIP multi-model mean because it is often considered as the best estimate for future climate as individual model biases are partly cancelled (Knutti et al., 2010). The use of future anomalies with respect to present day is expected to remove a part of the biases in individual model projections given that the CMIP model biases are largely stationary even under strong climate changes (Krinner & Flanner, 2018), while conserving linearities like the geostrophic balance. Besides, the numerical cost of each  $1/12^\circ$  ocean simulation precludes forcing them by each of the 33 CMIP5 models for both present and future conditions. However, an important limitation of our projection method is that we do not account for possible changes

317 in the frequency of interannual events like El Niño (Cai et al., 2014), and it will be im-  
318 portant to confront our results to direct downscaling of the CMIP models. Finally, we  
319 have chosen to force our ocean simulations using a 10 km regional atmospheric model,  
320 which is expected to be more realistic along the coastline and the shelf break than the  
321 much coarser CMIP models (e.g., Dinniman et al., 2015; Huot et al., 2021), although the  
322 use of such an intermediate model may be an additional source of biases and uncertainty  
323 in the chain of projections. The regional atmosphere model (MAR) is nonetheless renowned  
324 for its representation of polar processes in the Antarctic coastal region (e.g., Donat-Magnin  
325 et al., 2020; Mottram et al., 2021; Kittel et al., 2022), while most CMIP models have rep-  
326 resentations of snow, clouds and surface boundary layers that are less accurate in pol-  
327 ar regions (e.g., Lenaerts et al., 2016, 2017). Yet, it will be important to explore other  
328 projection methods to confirm the results of this study.

329 All our conclusions are nonetheless based on a single ocean model, even if we used  
330 three different set-ups, and it will be important to challenge these results using differ-  
331 ent ocean models. Our 1/12° resolution enables the resolution of eddies in the South-  
332 ern Ocean, which is key to simulating future sea ice decline (Rackow et al., 2022) and  
333 future heat transport towards Antarctica (van Westen & Dijkstra, 2021). This resolu-  
334 tion is also sufficient for the resolution of mean flow topography interactions involved in  
335 bringing CDW onto the continental shelf (St-Laurent et al., 2013), but not sufficient to  
336 resolve eddies on the continental shelf and within ice shelf cavities (Stewart et al., 2018,  
337 e.g.), or the interaction between Rossby waves along the shelf break and bathymetric  
338 troughs (St-Laurent et al., 2013). It remains difficult to estimate the role of these small  
339 scales on the evolution of heat transport towards the ice shelf cavities of the Amundsen  
340 Sea as previous high-resolution studies did not represent fine-scale bathymetry and ice  
341 shelf cavities in the Amundsen Sea (Stewart et al., 2018). Another important limitation  
342 of our modelling approach is that there is no ice sheet model coupled to NEMO in this  
343 study, i.e., ice shelves are static. This was shown to be an important limitation (Donat-  
344 Magnin et al., 2017), albeit for much stronger and longer melt perturbations.

345 Finally, given that the Antarctic Ice Sheet projections show the highest sensitiv-  
346 ity to increased basal melt rates in the Amundsen Sea sector (Seroussi et al., 2020), our  
347 regional results can provide a critical perspective on the Antarctic contribution to the  
348 21<sup>st</sup> century sea level rise simulated within ISMIP6 (Seroussi et al., 2020) and emulated  
349 by Edwards et al. (2021). The high-end estimates for 2100 under RCP8.5 (~30 cm of  
350 additional sea level) were obtained from the 95<sup>th</sup> percentile of the PIGL parameters, which  
351 we find highly incompatible with our simulations. Edwards et al. (2021) empirically de-  
352 fined a continuous distribution of  $K$  coefficients (their Fig. 3d), with a relatively large  
353 cumulative probability around the median PIGL parameter, and low-probability extreme  
354 values beyond the 95<sup>th</sup> percentile of PIGL parameters. Our projections suggest that this  
355 distribution should be narrowed towards lower values and that lower parameters should  
356 be used even for risk averse projections.

## 357 **Data and softwares**

358 The model version and set of parameters used to run our experiments are provided  
359 in <https://doi.org/10.5281/zenodo.6644859>. All the python scripts used to build  
360 the figures are provided in [http://github.com/nicojourdain/SCRIPTS\\_PAPER\\_PLOTS](http://github.com/nicojourdain/SCRIPTS_PAPER_PLOTS)  
361 and are mainly based on the Xarray (Hoyer & Hamman, 2017), Numpy (Harris et al.,  
362 2020) and Matplotlib (Hunter, 2007) packages. THE GITHUB REPOSITORIES WILL  
363 BE ARCHIVED ON <http://zenodo.org> AFTER ACCEPTANCE.

## 364 **Acknowledgments**

365 This publication is PROTECT contribution number XX. This study was funded by the  
366 European Union’s Horizon 2020 research and innovation programme under grant agree-

367 ments No 869304 (PROTECT), No 820575 (TiPACCs) and No 101003826 (CRiceS). It  
 368 was also partly funded by the French National Research Agency under grant No ANR-  
 369 19-CE01-0015 (EIS). This work was granted access to the HPC resources of CINES un-  
 370 der the allocation A0100106035 attributed by GENCI.

## 371 References

- 372 Asay-Davis, X. S., Jourdain, N. C., & Nakayama, Y. (2017). Developments in Sim-  
 373 ulating and Parameterizing Interactions Between the Southern Ocean and the  
 374 Antarctic Ice Sheet. *Current Climate Change Reports*, 3(4), 316–329.
- 375 Bett, D. T., Holland, P. R., Naveira Garabato, A. C., Jenkins, A., Dutrieux, P.,  
 376 Kimura, S., & Fleming, A. (2020). The impact of the Amundsen Sea freshwa-  
 377 ter balance on ocean melting of the West Antarctic Ice Sheet. *J. Geophys. Res.*  
 378 *Oceans*, 125(9), e2020JC016305.
- 379 Budge, J. S., & Long, D. G. (2018). A comprehensive database for Antarctic iceberg  
 380 tracking using scatterometer data. *IEEE Journal of Selected Topics in Applied*  
 381 *Earth Observations and Remote Sensing*, 11(2), 434–442.
- 382 Burgard, C., Jourdain, N. C., Reese, R., Jenkins, A., & Mathiot, P. (2022). An  
 383 assessment of basal melt parameterisations for Antarctic ice shelves. *The*  
 384 *Cryosphere Discussion*, 0, 0–0.
- 385 Cai, W., Borlace, S., Lengaigne, M., Van Rensch, P., Collins, M., Vecchi, G., ...  
 386 others (2014). Increasing frequency of extreme El Niño events due to green-  
 387 house warming. *Nat. Clim. Change*, 4(2), 111–116.
- 388 DeConto, R. M., Pollard, D., Alley, R. B., Velicogna, I., Gasson, E., Gomez, N., ...  
 389 others (2021). The Paris Climate Agreement and future sea-level rise from  
 390 Antarctica. *Nature*, 593(7857), 83–89.
- 391 Dinniman, M. S., Klinck, J. M., Bai, L.-S., Bromwich, D. H., Hines, K. M., & Hol-  
 392 land, D. M. (2015). The Effect of Atmospheric Forcing Resolution on Delivery  
 393 of Ocean Heat to the Antarctic Floating Ice Shelves. *J. Climate*, 28(15),  
 394 6067–6085.
- 395 Donat-Magnin, M., Jourdain, N. C., Gallée, H., Amory, C., Kittel, C., Fettweis,  
 396 X., ... Agosta, C. (2020). Interannual Variability of Summer Surface Mass  
 397 Balance and Surface Melting in the Amundsen Sector, West Antarctica. *The*  
 398 *Cryosphere*, 14(1), 229–249.
- 399 Donat-Magnin, M., Jourdain, N. C., Kittel, C., Agosta, C., Amory, C., Gallée, H.,  
 400 ... Chekki, M. (2021). Future surface mass balance and surface melt in the  
 401 Amundsen sector of the West Antarctic Ice Sheet. *The Cryosphere*, 15(2),  
 402 571–593.
- 403 Donat-Magnin, M., Jourdain, N. C., Spence, P., Le Sommer, J., Gallée, H., & Du-  
 404 rand, G. (2017). Ice-Shelf Melt Response to Changing Winds and Glacier  
 405 Dynamics in the Amundsen Sea Sector, Antarctica. *J. Geophys. Res.*, 122(12),  
 406 10206–10224.
- 407 Durand, G., van den Broeke, M. R., Le Cozannet, G., Edwards, T. L., Holland,  
 408 P. R., Jourdain, N. C., ... others (2022). Sea-level rise: From global perspec-  
 409 tives to local services. *Frontiers in marine science*, 2088.
- 410 Dutrieux, P., De Rydt, J., Jenkins, A., Holland, P. R., Ha, H. K., Lee, S. H., ...  
 411 Schröder, M. (2014). Strong sensitivity of Pine Island ice-shelf melting to  
 412 climatic variability. *Science*, 343(6167), 174–178.
- 413 Edwards, T. L., Nowicki, S., Marzeion, B., Hock, R., Goelzer, H., Seroussi, H., ...  
 414 others (2021). Projected land ice contributions to twenty-first-century sea level  
 415 rise. *Nature*, 593(7857), 74–82.
- 416 Eyring, V., Bony, S., Meehl, G. A., Senior, C. A., Stevens, B., Stouffer, R. J., &  
 417 Taylor, K. E. (2016). Overview of the Coupled Model Intercomparison Project  
 418 Phase 6 (CMIP6) experimental design and organization. *Geosci. Model Dev.*,  
 419 9(5), 1937–1958.

- 420 Favier, L., Jourdain, N. C., Jenkins, A., Merino, N., Durand, G., Gagliardini, O., ...  
 421 Mathiot, P. (2019). Assessment of Sub-Shelf Melting Parameterisations Using  
 422 the Ocean-Ice Sheet Coupled Model NEMO (v3. 6)-Elmer/Ice (v8. 3). *Geosci.*  
 423 *Model Dev.*
- 424 Fox-Kemper, B., Hewitt, H., Xiao, C., Aalgeirsdóttir, G., Drijfhout, S. S., Edwards,  
 425 T. L., ... Yu, Y. (2021). Ocean, Cryosphere and Sea Level Change. In *Climate*  
 426 *Change 2021: The Physical Science Basis. Contribution of Working Group*  
 427 *I to the Sixth Assessment Report of the Intergovernmental Panel on Climate*  
 428 *Change* (pp. 1211–1362). Cambridge University Press, Cambridge, United  
 429 Kingdom and New York, NY, USA. doi: 10.1017/9781009157896.011
- 430 Gallée, H., & Schayes, G. (1994). Development of a three-dimensional meso- $\gamma$  primi-  
 431 tive equation model: katabatic winds simulation in the area of Terra Nova Bay,  
 432 Antarctica. *Monthly Wea. Rev.*, *122*(4), 671–685.
- 433 Goyal, R., Sen Gupta, A., Jucker, M., & England, M. H. (2021). Historical and  
 434 projected changes in the southern hemisphere surface westerlies. *Geophys. Res.*  
 435 *Lett.*, *48*(4), e2020GL090849.
- 436 Harris, C. R., Millman, K. J., van der Walt, S. J., Gommers, R., Virtanen, P.,  
 437 Cournapeau, D., ... others (2020). Array programming with NumPy.  
 438 *Nature*, *585*(7825), 357–362. Retrieved from [https://doi.org/10.1038/](https://doi.org/10.1038/s41586-020-2649-2)  
 439 [s41586-020-2649-2](https://doi.org/10.1038/s41586-020-2649-2) doi: 10.1038/s41586-020-2649-2
- 440 Hausfather, Z., & Peters, G. P. (2020a). Emissions-the business as usual’s story is mis-  
 441 leading. *Nature*, *577*(7792), 618–620.
- 442 Hausfather, Z., & Peters, G. P. (2020b). RCP8. 5 is a problematic scenario for near-  
 443 term emissions. *Proc. Natl. Acad. Sci. U.S.A.*, *117*(45), 27791–27792.
- 444 Hinkel, J., Church, J. A., Gregory, J. M., Lambert, E., Le Cozannet, G., Lowe, J.,  
 445 ... van de Wal, R. (2019). Meeting user needs for sea level rise information: a  
 446 decision analysis perspective. *Earth’s Future*, *7*(3), 320–337.
- 447 Holland, P. R., Bracegirdle, T. J., Dutrieux, P., Jenkins, A., & Steig, E. J. (2019).  
 448 West Antarctic ice loss influenced by internal climate variability and anthro-  
 449 pogenic forcing. *Nature Geoscience*, 1–7.
- 450 Holland, P. R., Jenkins, A., & Holland, D. M. (2008). The response of ice shelf basal  
 451 melting to variations in ocean temperature. *J. Climate*, *21*(11), 2558–2572.
- 452 Hoyer, S., & Hamman, J. (2017). xarray: N-D labeled arrays and datasets in  
 453 Python. *J. Open Res. Softw.*, *5*(1). Retrieved from [https://doi.org/](https://doi.org/10.5334/jors.148)  
 454 [10.5334/jors.148](https://doi.org/10.5334/jors.148) doi: 10.5334/jors.148
- 455 Hunter, J. D. (2007). Matplotlib: A 2D graphics environment. *Computing in Science*  
 456 *& Engineering*, *9*(3), 90–95. doi: 10.1109/MCSE.2007.55
- 457 Huot, P.-V., Kittel, C., Fichet, T., Jourdain, N. C., Sterlin, J., & Fettweis, X.  
 458 (2021). Effects of the atmospheric forcing resolution on simulated sea ice and  
 459 polynyas off Adélie Land, East Antarctica. *Ocean Modelling*, *168*, 101901.
- 460 Jenkins, A., Shoosmith, D., Dutrieux, P., Jacobs, S., Kim, T. W., Lee, S. H., ...  
 461 Stammerjohn, S. (2018). West Antarctic Ice Sheet retreat in the Amundsen  
 462 Sea driven by decadal oceanic variability. *Nature Geosc.*, *11*, 733–738.
- 463 Jourdain, N. C., Asay-Davis, X., Hattermann, T., Straneo, F., Seroussi, H., Little,  
 464 C. M., & Nowicki, S. (2020). A protocol for calculating basal melt rates in the  
 465 ISMIP6 Antarctic ice sheet projections. *The Cryosphere*, *14*(9), 3111–3134.
- 466 Jourdain, N. C., Mathiot, P., Merino, N., Durand, G., Le Sommer, J., Spence, P.,  
 467 ... Madec, G. (2017). Ocean circulation and sea-ice thinning induced by  
 468 melting ice shelves in the Amundsen Sea. *J. Geophys. Res. Oceans*, *122*(3),  
 469 2550–2573.
- 470 Jourdain, N. C., Merino, N., Le Sommer, J., Durand, G., & Mathiot, P. (2019). *In-*  
 471 *terannual iceberg meltwater fluxes over the Southern Ocean (1.0)* (Tech. Rep.).  
 472 Retrieved from <https://doi.org/10.5281/zenodo.3514728>
- 473 Jourdain, N. C., Molines, J.-M., Le Sommer, J., Mathiot, P., Chanut, J., de  
 474 Lavergne, C., & Madec, G. (2019). Simulating or prescribing the influence

- 475 of tides on the Amundsen Sea ice shelves. *Ocean Modelling*, 133, 44–55.
- 476 Kittel, C., Amory, C., Hofer, S., Agosta, C., Jourdain, N. C., Gilbert, E., ... Fet-  
477 tweis, X. (2022). Clouds drive differences in future surface melt over the  
478 Antarctic ice shelves. *The Cryosphere*, 16(7), 2655–2669.
- 479 Knutti, R., Furrer, R., Tebaldi, C., Cermak, J., & Meehl, G. A. (2010). Challenges  
480 in combining projections from multiple climate models. *J. Climate*, 23(10),  
481 2739–2758.
- 482 Krinner, G., & Flanner, M. G. (2018). Striking stationarity of large-scale climate  
483 model bias patterns under strong climate change. *Proceedings of the National  
484 Academy of Sciences*, 115(38), 9462–9466.
- 485 Lenaerts, J. T. M., Van Tricht, K., Lhermitte, S., & L’Ecuyer, T. S. (2017). Polar  
486 clouds and radiation in satellite observations, reanalyses, and climate models.  
487 *Geophys. Res. Lett.*, 44(7), 3355–3364.
- 488 Lenaerts, J. T. M., Vizcaino, M., Fyke, J., Van Kampenhout, L., & van den Broeke,  
489 M. R. (2016). Present-day and future Antarctic ice sheet climate and surface  
490 mass balance in the Community Earth System Model. *Clim. Dyn.*, 47(5-6),  
491 1367–1381.
- 492 Levermann, A., Winkelmann, R., Albrecht, T., Goelzer, H., Golledge, N. R., Greve,  
493 R., ... others (2020). Projecting Antarctica’s contribution to future sea level  
494 rise from basal ice shelf melt using linear response functions of 16 ice sheet  
495 models (LARMIP-2). *Earth System Dynamics*, 11(1), 35–76.
- 496 Madec, G., & NEMO-team. (2016). *NEMO ocean engine, version 3.6 stable, Note  
497 du Pôle de modélisation de l’Institut Pierre-Simon Laplace No 27, ISSN No  
498 1288-1619* (Tech. Rep.). IPSL, France.
- 499 Mathiot, P., Jenkins, A., Harris, C., & Madec, G. (2017). Explicit and parametrised  
500 representation of under ice shelf seas in az\* coordinate ocean model NEMO  
501 3.6. *Geosci. Model Dev.*, 10(7), 2849–2874.
- 502 Merino, N., Jourdain, N. C., Le Sommer, J., Goosse, H., Mathiot, P., & Durand, G.  
503 (2018). Impact of increasing antarctic glacial freshwater release on regional  
504 sea-ice cover in the Southern Ocean. *Ocean Model.*, 121, 76–89.
- 505 Merino, N., Le Sommer, J., Durand, G., Jourdain, N. C., Madec, G., Mathiot, P.,  
506 & Tournadre, J. (2016). Antarctic icebergs melt over the Southern Ocean :  
507 climatology and impact on sea-ice. *Ocean Model.*, 104, 99–110.
- 508 Morlighem, M. (2020). *MEASUREs BedMachine Antarctica, Version 2* (Tech.  
509 Rep.). Boulder, Colorado USA. NASA National Snow and Ice Data Center  
510 Distributed Active Archive Center. Retrieved from [https://nsidc.org/data/  
511 NSIDC-0756/versions/2](https://nsidc.org/data/NSIDC-0756/versions/2) doi: 10.5067/E1QL9HFQ7A8M
- 512 Morlighem, M., Rignot, E., Binder, T., Blankenship, D., Drews, R., Eagles, G., ...  
513 others (2020). Deep glacial troughs and stabilizing ridges unveiled beneath the  
514 margins of the Antarctic ice sheet. *Nature Geoscience*, 13(2), 132–137.
- 515 Mottram, R., Hansen, N., Kittel, C., van Wessem, J. M., Agosta, C., Amory, C.,  
516 ... others (2021). What is the surface mass balance of Antarctica? An in-  
517 tercomparison of regional climate model estimates. *The Cryosphere*, 15(8),  
518 3751–3784.
- 519 Nakayama, Y., Menemenlis, D., Zhang, H., Schodlok, M., & Rignot, E. (2018).  
520 Origin of Circumpolar Deep Water intruding onto the Amundsen and Belling-  
521 shausen Sea continental shelves. *Nat. Comm.*, 9(1), 1–9.
- 522 Nakayama, Y., Timmermann, R., Schröder, M., & Hellmer, H. H. (2014). On the  
523 difficulty of modeling Circumpolar Deep Water intrusions onto the Amundsen  
524 Sea continental shelf. *Ocean Model.*, 84, 26–34.
- 525 Naughten, K. A., Holland, P. R., Dutrieux, P., Kimura, S., Bett, D. T., & Jenkins,  
526 A. (2022). Simulated twentieth-century ocean warming in the Amundsen Sea,  
527 West Antarctica. *Geophys. Res. Lett.*, e2021GL094566.
- 528 Naughten, K. A., Meissner, K. J., Galton-Fenzi, B. K., England, M. H., Timmer-  
529 mann, R., & Hellmer, H. H. (2018). Future projections of Antarctic ice shelf

- 530 melting based on CMIP5 scenarios. *J. Climate*, *31*(13), 5243–5261.
- 531 Naughten, K. A., Meissner, K. J., Galton-Fenzi, B. K., England, M. H., Timmer-  
532 mann, R., Hellmer, H. H., . . . Debernard, J. B. (2018). Intercomparison of  
533 Antarctic ice-shelf, ocean, and sea-ice interactions simulated by MetROMS-  
534 iceshelf and FESOM 1.4. *Geosci. Model Dev.*, *11*(4), 1257–1292.
- 535 Nowicki, S., Payne, A., Goelzer, H., Seroussi, H., Lipscomb, W., Abe-Ouchi, A., . . .  
536 van de Wal, R. (2020). Experimental protocol for sea level projections from  
537 ISMIP6 standalone ice sheet models. *The Cryosphere*, *14*, 2331–2368. doi:  
538 10.5194/tc-14-2331-2020
- 539 Purich, A., & England, M. H. (2021). Historical and future projected warming of  
540 Antarctic Shelf Bottom Water in CMIP6 models. *Geophys. Res. Lett.*, *48*(10),  
541 e2021GL092752.
- 542 Rackow, T., Danilov, S., Goessling, H. F., Hellmer, H. H., Sein, D. V., Semmler,  
543 T., . . . Jung, T. (2022). Delayed Antarctic sea-ice decline in high-resolution  
544 climate change simulations. *Nature Comm.*, *13*(1), 1–12.
- 545 Rousset, C., Vancoppenolle, M., Madec, G., Fichefet, T., Flavoni, S., Barthélemy,  
546 A., . . . others (2015). The Louvain-La-Neuve sea ice model LIM3.6: global and  
547 regional capabilities. *Geosci. Model Dev.*, *8*(10), 2991–3005.
- 548 Seroussi, H., Nowicki, S., Payne, A. J., Goelzer, H., Lipscomb, W. H., Abe-Ouchi,  
549 A., . . . others (2020). ISMIP6 Antarctica: a multi-model ensemble of the  
550 Antarctic ice sheet evolution over the 21st century. *The Cryosphere*, *14*(9),  
551 3033–3070.
- 552 Siahaan, A., Smith, R., Holland, P., Jenkins, A., Gregory, J. M., Lee, V., . . . Jones,  
553 C. (2021). The Antarctic contribution to 21st century sea-level rise predicted  
554 by the UK Earth System Model with an interactive ice sheet. *The Cryosphere*  
555 *Discussions*, 1–42.
- 556 Smith, R. S., Mathiot, P., Siahaan, A., Lee, V., Cornford, S. L., Gregory, J. M., . . .  
557 others (2021). Coupling the UK Earth System Model to dynamic models  
558 of the Greenland and Antarctic ice sheets. *J. Adv. Model. Ea. Sys.*, *13*(10),  
559 e2021MS002520.
- 560 Spence, P., Griffies, S. M., England, M. H., Hogg, A. M., Saenko, O. A., & Jourdain,  
561 N. C. (2014). Rapid subsurface warming and circulation changes of Antarctic  
562 coastal waters by poleward shifting winds. *Geophys. Res. Lett.*, *41*(13),  
563 4601–4610.
- 564 Stewart, A. L., Klocker, A., & Menemenlis, D. (2018). Circum-Antarctic Shoreward  
565 Heat Transport Derived From an Eddy-and Tide-Resolving Simulation. *Geo-*  
566 *phys. Res. Lett.*, *45*(2), 834–845. doi: 10.1002/2017GL075677
- 567 St-Laurent, P., Klinck, J. M., & Dinniman, M. S. (2013). On the role of coastal  
568 troughs in the circulation of warm Circumpolar Deep Water on Antarctic  
569 shelves. *J. Phys. Oceanogr.*, *43*(1), 51–64.
- 570 Swart, N. C., & Fyfe, J. C. (2012). Observed and simulated changes in the Southern  
571 Hemisphere surface westerly wind-stress. *Geophys. Res. Lett.*, *39*(16).
- 572 Timmermann, R., & Hellmer, H. H. (2013). Southern Ocean warming and increased  
573 ice shelf basal melting in the twenty-first and twenty-second centuries based on  
574 coupled ice-ocean finite-element modelling. *Ocean Dyn.*, *63*(9-10), 1011–1026.
- 575 van Westen, R. M., & Dijkstra, H. A. (2021). Ocean eddies strongly affect global  
576 mean sea-level projections. *Science Adv.*, *7*(15), eabf1674.
- 577 Williamson, D. B., Blaker, A. T., & Sinha, B. (2017). Tuning without over-tuning:  
578 parametric uncertainty quantification for the NEMO ocean model. *Geosci.*  
579 *Model Dev.*, *10*(4), 1789–1816.